PROCESS MODELLING OF THE ELECTRON BEAM WELDING OF AEROENGINE COMPONENTS

R. C. Reed, H.J. Stone, D Dye and S.M. Roberts

Department of Materials Science and Metallurgy/Rolls-Royce University Technology Centre,
University of Cambridge, Cambridge, CB2 3QZ, UK.

S. G. McKenzie

Rolls-Royce plc.,
PO Box 31, Elton Road, Derby, DE24 8BJ, UK.

Abstract

A numerical process model is described for the prediction of residual stresses and distortion arising from the electron beam welding of Waspaloy. Simulations have been conducted with this model for welds performed at a number of focal positions of the electron beam. Comparison is made between the model predictions and experimental measurements of the thermal cycles, the residual stresses and distortion. Good agreement is observed between the model and experiment for the thermal cycles and residual stresses. Distortion can also be predicted but some discrepancies have been noted.

Introduction

Electron beam welding (EBW) [1] is used widely by gas turbine manufacturers for the fabrication of compressor assemblies. A photograph of a typical component and a close-up of the weld is given in Figure 1. Successful processing relies on the careful generation and manipulation of a high power electron beam, which provides power densities at the work-piece surface in excess of $10^{10}\,\mathrm{W\,m^{-2}}$ [2]. At these power densities, a near cylindrical cavity of vapour or 'key-hole' is produced which may extend to considerable depths into the work-piece [3]. This characteristic enables autogenous welding to be accomplished on thick sectioned components in a single welding pass. Furthermore, as energy may be deposited almost uniformly through the depth of the key-hole, the post-welding distortions produced are typically smaller than those produced by more conventional fusion welding processes [4].

Nevertheless, considerable care is required when using electron beam welding for the manufacture of compressor assemblies, particularly in nickel-base alloys, for a number of reasons. First, the distortions that are generated by welding, whilst small, can be close to the limits that can be tolerated. Excessive distortion necessitates costly reworking or scrapping of the components. Second, as the structural integrity of these components must be ensured, reliable estimates of the residual stresses generated by welding need to be obtained for calculations of projected component life. Such estimates are often made via residual stress measurement techniques which are destructive. Finally, selection and optimisation of process parameters such that post-weld distortions are minimised, has traditionally involved a considerable amount of experimentation on a trial-and-error basis. Such strategies are highly reliant on the expertise of welding engineers and can often be inefficient, particularly when high strength alloys such as superalloys are employed.

The field of computational weld mechanics now offers the possibility of using numerical models to perform weld investigations virtually, *i.e.* on the computer. These models employ finite element codes to obtain a piece-wise polynomial solution to the differential equations governing heat transfer and the mechanical response of the component geometry to the applied thermal and mechanical loads. However, it should be noted that considerable experimentation is required during the development of these models for the purpose of calibration and validation. In the present paper, a numerical process model for the electron beam welding of Waspaloy is presented. The results obtained are compared with data obtained with a number of experimental techniques. The advantages and limitations of the approach are identified.

Numerical Modelling

The numerical model was constructed with the aim of providing a predictive capability for the residual stresses and distortions that arise as a consequence of the electron beam welding of Waspaloy. In such a model, the desire to incorporate as much of the process physics as possible must be balanced against the implementation and validation costs. As a consequence, a pragmatic decision was made to circumvent the complex physical processes that occur in the weld pool and to approximate the deposition of heat into the work-piece by an arbitrary volumetric heat generation rate.

Superalloys 2000
Edited by T.M. Pollock, R.D.,Kissinger, R.R. Bowman,
K.A. Green, M. McLean, S. Olson, and J.J. Schirra
TMS (The Minerals, Metals & Materials Society), 2000

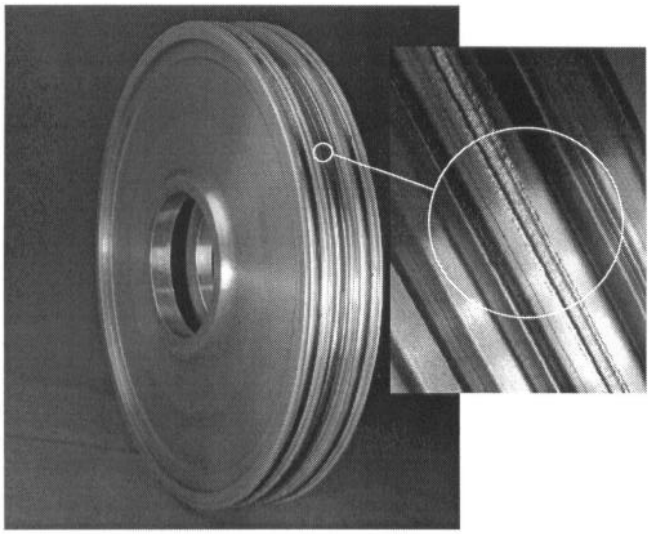

Figure 1: Photograph of an aeroengine compressor assembly with a close-up of the electron beam weld.

The computations have been performed as sequential thermal and mechanical analyses so that the transient thermal cycles generated by the moving heat source are used as the input for an elastic-plastic continuum mechanics-based solution for the strains, displacements and stresses. The division of the computation into separate thermal and mechanical analyses is deemed to be acceptable as the heat generated by the adiabatic heating of the material from the temperature induced deformations is insignificant compared to the heat deposited by the heat source [5].

Mesh Generation

One of the principal difficulties encountered with the successful implementation of a weld model is that of scale [6,7]. The element size at the location of the heat source has to be sufficient to ensure that the amount of energy deposited into the plate in reality is matched by the model. Furthermore, the form of the heat source is important and the mesh should be sufficiently fine to represent this. The implication of such a criterion is that the size of elements required around the heat source is likely to be small compared to the length of the weld path. If the entire geometry were to be discretised with elements of this size, the resultant mesh would possess a very considerable number of elements. Analysis of such a model would be likely to prove intractable. To avoid this difficulty a form of adaptive remeshing has been devised in which the necessary refinement around the heat source is provided along a short section of the total length only with larger elements beyond [8]. This methodology relies on the division of the total analysis into a series of sub-analyses, each with their own associated mesh. In each sub-analysis, the heat source is traversed along the short distance with high local element refinement, thereby allowing the energy deposited by the heat source to be accurately captured. For the thermal analysis, the results of the last time step on a given mesh are then interpolated onto the mesh of the subsequent sub-analysis as the starting conditions for the new sub-analysis and the heat source allowed to traverse along the next refined region. For the mechanical analysis, in addition to passing the results obtained at the end of the previous sub-analysis, the thermal results for that sub-analysis are also required. Three consecutive meshes are shown in Figure 2.

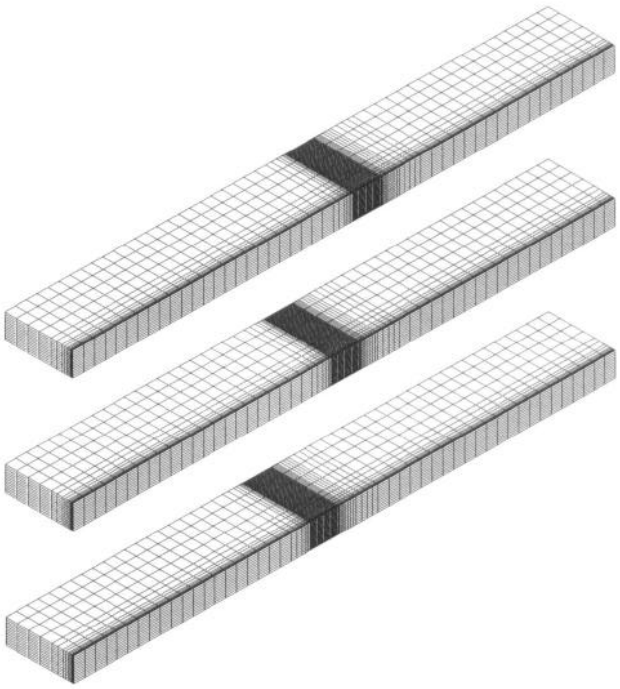

Figure 2: Three consecutive meshes used for the numerical analyses of welded test-plates.

To avoid incompatibility between the thermal and mechanical strain fields [9], linear elements have been used in the thermal analyses and quadratic elements with reduced integration in the mechanical analyses. The use of such elements in the mechanical analyses has the added advantage that it avoids the problems of volumetric and shear locking encountered with other element types [10].

Thermal Analysis

The deposition of heat into the work-piece geometry has been modelled by a linear combination of two distributed heat generation rates; that of a uniform circular surface flux and a uniform conical volumetric flux. Given a rectilinear plate such as that used in this investigation, with dimensions X, Y and Z in the Cartesian co-ordinate system (x, y, z) and with the sources moving at a constant velocity, v, in the yz-plane in the X-direction, the two source strengths, $\dot{Q}_{\text{surface}}$ and $\dot{Q}_{\text{volume}}$ are given by

$$\dot{Q}_{\text{surface}}\{\xi, y, 0\} = q_{\text{surface}} \quad \text{for } \xi^2 + y^2 \leq a^2_{\text{surface}} \tag{1}$$

and

$$\dot{Q}_{\text{volume}}\{\xi, y, z\} = q_{\text{volume}} \tag{2}$$

$$\text{for } \xi^2 + y^2 \leq (mz + a_{\text{volume}})^2 \text{ and } z \leq d$$

where $\xi = x - vt$, in which t is the welding time, q_{surface} and q_{volume} are the surface and volume fluxes corresponding to the two sources, a_{surface} and a_{volume} are the characteristic radii of the two terms, m is the gradient of the conic decrease in width of the volume term and d is the penetration depth of the electron beam, which equals the thickness of the plate in the fully penetrating condition.

From the conservation of energy, the total power delivered by the two heat source terms must equal that provided by the electron beam. If a partitioning ratio, r, is defined as the proportion of the total power delivered to the surface term then

$$q_{\text{surface}} = \frac{r\eta VI}{\pi a_{\text{surface}}^2} \tag{3}$$

and

$$q_{\text{volume}} = \frac{(1-r)\eta VI}{\pi d\left(\frac{1}{3}m^2d^2 + mda_{\text{volume}} + a_{\text{volume}}^2\right)} \tag{4}$$

where VI is the power supplied to the electron beam and η is the experimentally determined coupling efficiency.

The parameters a_{surface}, a_{volume}, m and r cannot be measured directly and instead must be optimised by comparison with the weld fusion boundary profiles and thermocouple data. To achieve this, a series of single step analyses were performed in the Eulerian reference frame. The solidus isotherm from the model was then compared with the fusion boundary profile and the parameters refined until good agreement between the two was achieved.

Once all of these modelling parameters were acquired, the full thermal transient analysis could be performed. This was conducted using the Broyden-Fletcher-Goldfarb-Shanno inverse update (BFGS) iteration method [11]. The calculation was continued until the model had achieved a uniform saturation temperature; after which, forced cooling of the model to ambient temperature (25°C) was performed.

Mechanical Analysis

On completion of the thermal analysis, the nodal temperatures were transferred to the mechanical model. The model was performed as an elasto-plastic analysis with linear isotropic hardening. As with the thermal analysis, the BFGS iteration method was used.

The mechanical constraints imposed on the model consisted of: (i) a symmetry condition across the plane of nodes along the weld path; (ii) a pin joint at one end of the plate; (iii) a simple support at the other. These constraint conditions are consistent with the 'unconstrained' bead on plate welds performed, allowing free deformation of the plates during welding.

Weld Manufacture and Characterisation

Plate test pieces of the dimensions 200 × 50 × 9 mm were machined from Waspaloy. After machining, the plates were subjected to a vacuum heat treatment consisting of a 5 hour dwell at 760°C, followed by furnace cooling to ambient temperature. The purpose of this heat treatment was to alleviate the residual stresses generated by the prior manufacturing operations.

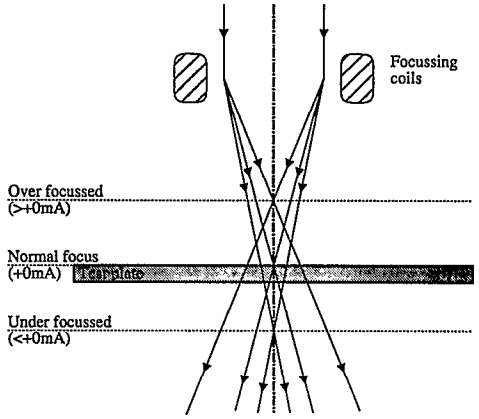

Figure 3: Schematic illustration of overfocussed, normal focussed and underfocussed electron beams

Autogenous bead-on-plate welding passes were conducted along the centre of each test-piece in the long direction of the plate using a Steigerwald K-100 electron beam welding machine with computer numeric control. The welds were conducted at ten different focal positions of the electron beam between the under-focussed and over-focussed conditions (Figure 3), with the remaining welding parameters being kept constant. The welding parameters used are given in Table I. In the following sections the samples have been referenced by the difference between the current in the focussing coils at which they were welded and the current required to achieve a normal focus.

Tabel I Welding parameters used for the fabrication of the test-pieces investigated in this study

Voltage (kV)	Beam current (mA)	Velocity mm s^{-1}	Defocus (mA)
150	23	8.4	+90
150	23	8.4	+70
150	23	8.4	+50
150	23	8.4	+40
150	23	8.4	+30
150	23	8.4	+20
150	23	8.4	+10
150	23	8.4	+0
150	23	8.4	-20
150	23	8.4	-40

Measurement of Thermal Transients

In-situ monitoring of the thermal transients generated during the welding process was performed using surface mounted thermocouples attached to commercial data-logging equipment via a shielded extension cable. Additional noise reduction was achieved with the use of filtering in the data-logging software.

Metallographic Sectioning

Metallographic sections were prepared of each of the welds in the plane perpendicular to the direction of welding. Microstructural relief was achieved using Kalling's reagent (5 g $CuCl_2$, 100 ml HCl, 100 ml ethanol).

Characterisation of Weld-Induced Distortion

The post-weld distortion of the welded plates were determined from measurements made of the surface topography of the welded samples. These measurements were performed using a Leitz PMM12106 three-dimensional needle probe coordinate measurement device. By this method it was possible to identify and characterise the two principal distortion modes of the test-pieces: (a) angular distortion or 'butterflying', which is manifest as a bending of the test-pieces along the weld path; and, (b) camber distortion, occurring as a curvature of the test-pieces along the length of the weld. These distortion modes are shown schematically in Figure 4.

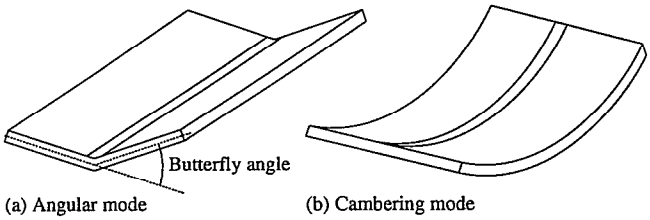

Figure 4: Schematic diagram of two principal distortion modes (a) angular distortion and, (b) camber distortion.

Residual Stress Determination

Measurements of the residual stress state in the plate welded at +20 mA defocus were conducted using neutron diffraction, X-ray diffraction and incremental hole-drilling methods. Comparisons made of the applicability of each of these three techniques to the measurement of residual stresses around electron beam welds in Waspaloy suggest that these techniques should be considered as complementary [12].

Neutron Diffraction Neutron diffraction measurements were conducted at the ISIS facility, Rutherford Appleton Laboratory, UK. Measurements were performed in a step-wise fashion across the centre of the test-piece perpendicular to the welding direction as illustrated in Figure 5. For the full determination of the strain tensor, six independent measurements of strain are required [12]. However, to minimise the time required at each measurement position, it was assumed that the principal strain directions lay along the x, y and z directions of the plate (see Figure 5). This necessitated the measurement of strain in these directions only. The experimental set-ups for the simultaneous measurements of the strains in the y & z and x & z directions (ε_y & ε_z and ε_x & ε_z) are shown in Figure 6. Spatial resolution was provided

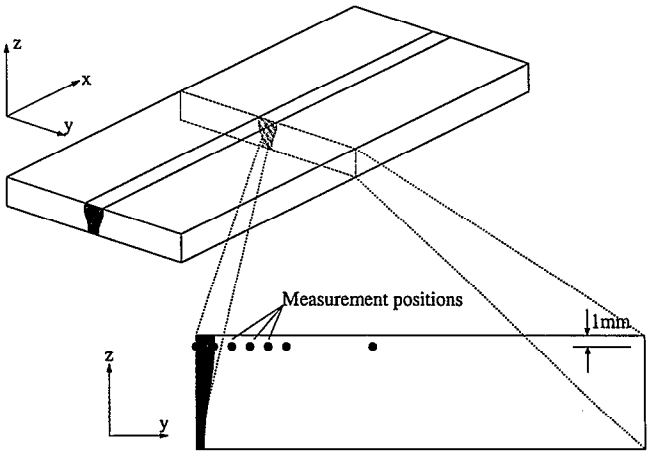

Figure 5: Schematic diagram of the test plate welded at +20 mA defocus illustrating the measurement locations used for the neutron diffraction measurements.

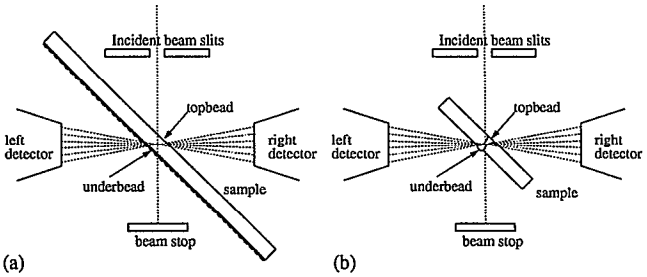

Figure 6: Experimental set-up for measurement of (a) ε_x & ε_z and (b) ε_y & ε_z.

by the use of slits 1×10 mm in the incident beam path for the measurements performed in the transverse and through-thickness directions and slits 2×2 mm for the measurements performed in the longitudinal and through thickness directions. These configurations gave illuminated gauge volumes of $1 \times 1.7 \times 10$ mm and $2 \times 1.7 \times 2$ mm respectively. The use of slits with different sizes for each of these measurement orientations was necessitated by the need to maximise the gauge volume in the sample and hence minimise the data collection time whilst ensuring that the spatial resolution remained sufficient to identify sharp variations in the stress field. The measurements were performed at a depth of 1 mm beneath the sample surface in order to ensure that the gauge volume was fully immersed in the sample in order to avoid edge effects. As the ISIS facility is a time-of-flight source, spectra containing all lattice reflections were obtained. The resultant spectra are composed principally of the overlaid diffraction patterns generated by the γ matrix and the γ' precipitates. As a result of the small lattice mismatch be-

tween these phases and the large intrinsic line widths it was not possible to resolve the reflections into their various phase constituents. However, it is believed that the treatment of the composite diffraction pattern as a single pattern does not generate erroneous results [13]. Consequently, the average strain in the sample was obtained by performing a Reitveld refinement on each full spectrum assuming only a single phase material. Conversion of the measured strains to stress could then be achieved using the bulk elastic modulus and Poisson's ratio. It is believed that this method provides an accurate measure of the macroscopic residual stress state, whilst overcoming the problems created by the presence of microstresses in the material [14].

X-ray Diffraction Measurements were also conducted by X-ray diffraction using a TEC 1610-2b dedicated residual stress measurement system. This system utilises a position sensitive proportional counter to capture the Bragg reflections from which the measurements are to be made. Calculation of the lattice strains is achieved using the $\sin^2\psi$ technique and the appropriate plane-specific diffraction elastic constants [15]. For the measurements performed in this study Cr-Kα radiation was employed, thus allowing access to the γ/γ' {220} lattice reflection at a fixed 2θ angle of approximately 128°. At each measurement position 6 ψ-tilts were used. Spatial resolution was provided by a 2 mm diameter circular collimator. The measurement positions used are illustrated schematically in Figure 7.

Hole-Drilling Incremental hole drilling measurements were carried out according to ASTM standard E-837-94 [16] by Stresscraft plc, Shepshed, Leicestershire, UK. In order that the region of relaxed stresses around a hole does not interfere with the next measurement made, a separation of greater than 15 mm was used between adjacent measurements. As a consequence, it was only possible to perform four individual measurements on the welded plate within the region in which the stresses are believed to be invariant [12].

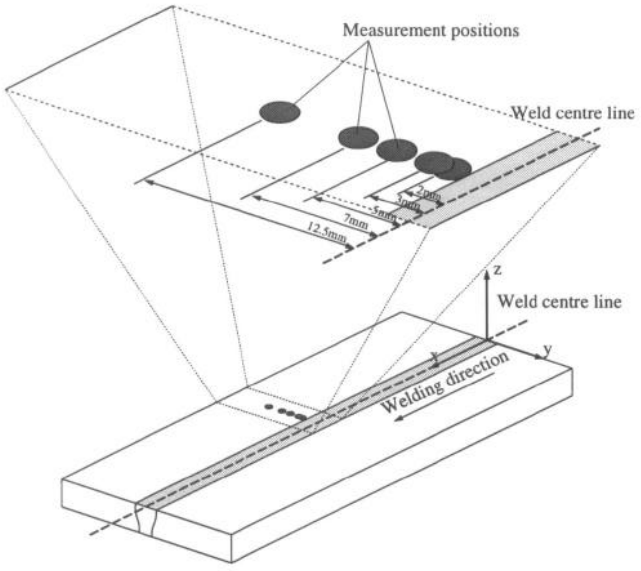

X–ray diffraction measurement positions at 2.0, 3.0, 5.0, 7.0 and 12.5 mm from the weld centre line

Figure 7: Schematic diagram of the test plate welded at +20 mA defocus illustrating the measurement locations used for the X-ray diffraction measurements.

Results and Discussion

Thermal Analysis The metallographic sections obtained from the welded samples are given in Figure 8. Acquisition of appropriate heat source parameters, a_{surface}, a_{volume}, m and r to model these welds was achieved by the manual variation of the parameters and comparison with the fusion boundary profiles, presented in Figure 9. The heat source parameters obtained in this fashion are given in Table II. As these heat source parameters were selected to provide the optimum agreement with the experimentally determined fusion boundary profiles, it is not surprising that good agreement was achieved between the model and the experiments.

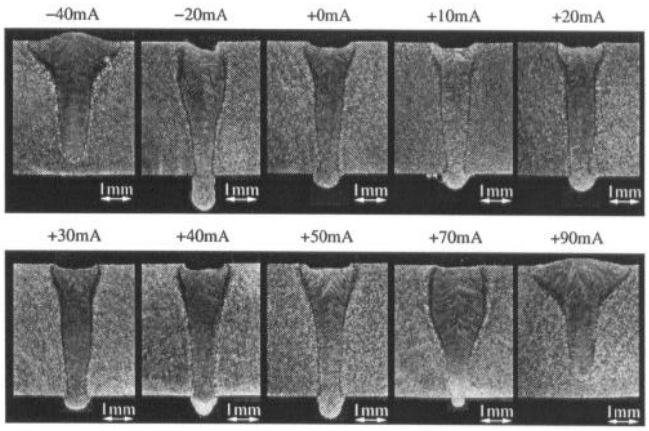

Figure 8: Metallographic sections from the bead-on-plate welds manufactured at different defocusses of the electron beam.

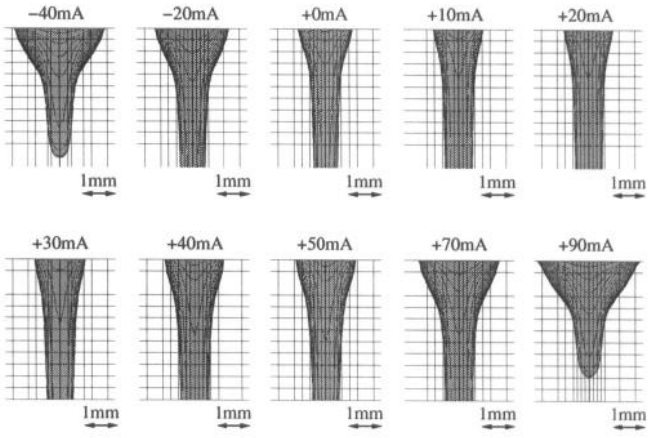

Figure 9: Predicted fusion boundaries obtained from the numerical model.

Table II Parameters used in the thermal model

Defocus (mA)	η	$a_{surface}$ (mm)	a_{volume} (mm)	m	r	d (mm)
+90	0.96	3.50	1.05	-0.025	0.35	7.7
+70	0.97	2.52	1.02	-0.0225	0.20	9
+50	0.88	1.76	1.0	-0.02	0.10	9
+40	0.88	1.79	1.0	-0.0175	0.10	9
+30	0.81	1.58	0.95	-0.015	0.075	9
+20	0.80	1.54	0.95	-0.013	0.075	9
+10	0.80	1.57	0.95	-0.013	0.075	9
+0	0.79	1.65	1.0	-0.015	0.10	9
-20	0.93	2.20	1.02	-0.02	0.20	9
-40	0.97	3.05	1.05	-0.025	0.30	8.7

A more stringent test of the thermal model is provided with comparison to the data acquired from the thermocouple measurements. The results obtained from the plates welded with normal focussed (+0 mA) and highly underfocussed (-40 mA) beams are presented in Figures 10 and 11. For the FEM results, two curves are plotted alongside each of the corresponding thermocouple results. These are representative of the upper and lower bounds of the predicted temperatures based upon the fact that the position of the thermocouple junctions could only be determined to within ±0.2 mm of these measured values. For all of the welding conditions investigated, excellent agreement was found between the FEM model and the thermocouple measurements. It can however be seen that the thermocouples appear to respond slower than the FEM results to the arrival of the heat source. This is likely to arise as a result of the finite separation of the thermocouple junctions. The measured temperature will therefore be some average of the temperature between these two points.

With these data it was also possible to extract an estimate of the thermal efficiency of the process, via the measurement of the uniform saturation temperature which each test-piece attained. The efficiencies obtained in this fashion are given in Table II.

For electron beam welding, it has been reported that the efficiency of energy coupling between the electron beam and the work-piece is typically 90-95% [1]. However, the efficiencies obtained from the thermocouple measurements, presented in Table II, are observed to decrease from 98% with the most defocused electron beams to 80% at the normal focus condition. This observation may be attributed to the fact that at all focal positions other than the most defocused, a fully penetrating weld cavity is produced. With full penetration, a proportion of the power supplied by the electron beam will pass through the work-piece and impinge on the fixture beyond. Additionally, as the normal focus condition is approached, so the incident power density will increase, and hence, a greater proportion of the power of the electron beam will be lost through the work-piece. Only in the cases of the non-penetrating welds generated with the most defocused electron beams is the true efficiency of energy coupling between the electron beam and the work-piece measured by this method.

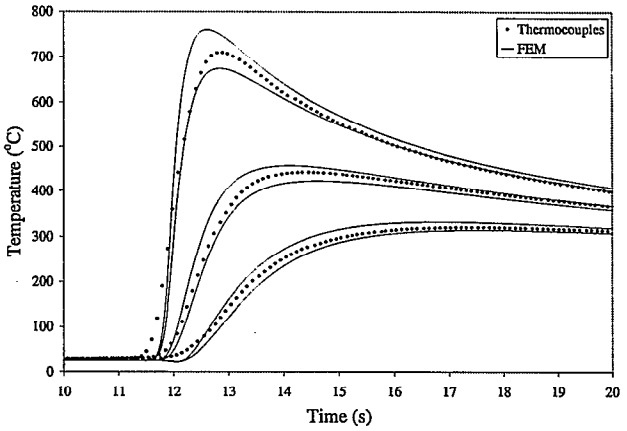

Figure 10: Thermal transients measured by surface mounted thermocouples and the associated upper and lower bound predictions from the associated numerical model for the test plate welded at +0 mA defocus.

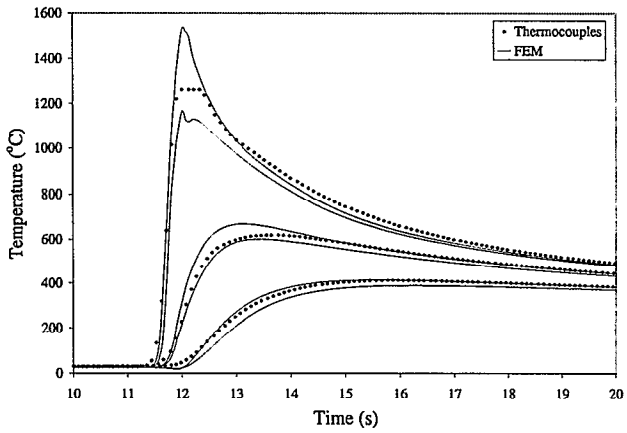

Figure 11: Thermal transients measured by surface mounted thermocouples and the associated upper and lower bound predictions from the associated numerical model for the test plate welded at -40 mA defocus.

Mechanical Analysis Contour plots of the longitudinal and transverse stress distributions predicted by the numerical model in the plane perpendicular to the welding direction at the centre of the plate are given in Figure 12. It can be seen that both stress components exhibit variations with depth into the sample. With the longitudinal stress component, the region of tensile stress is observed to be wider than with a lower peak stress at the surface of the plate than at depth. The transverse stress component exhibits greater variation still with compressive regions being seen at the surfaces of the plate in the weld and tensile stresses at depth.

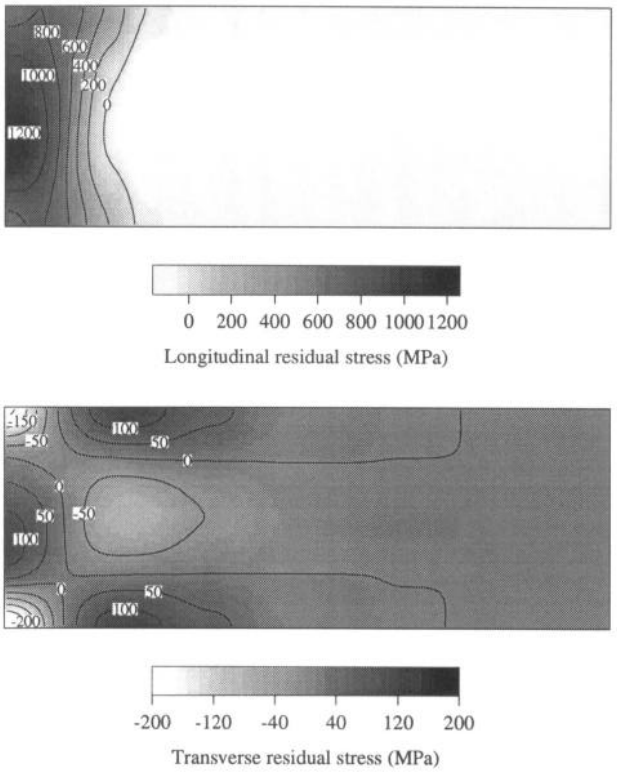

Figure 12: Contour plots of the longitudinal and transverse residual stresses across the centre of the model perpendicular to the weld.

The predicted and measured residual stresses across the plate perpendicular to the welding direction are shown in Figures 13 and 14. With the variations with depth identified in Figure 12 it is not appropriate to compare directly the residual stresses measured by the neutron diffraction technique at 1 mm into the sample with those obtained from the surface by X-ray diffraction and incremental hole-drilling. As a result, two lines have been plotted from the predictions made with the numerical model. The first line corresponds to the stresses predicted at the top surface of the plate, from which comparison with the stresses measured by the X-ray and hole-drilling methods may be made and the second line corresponds to those stresses predicted at a depth of 2.25 mm below the top surface. This has been selected as providing the approximate extent of penetration of the gauge volume used in the neutron diffraction measurements. If the upper limit of the gauge volume is assumed to lie at the surface of the sample, the neutron diffraction results would be expected to be bounded by the two lines.

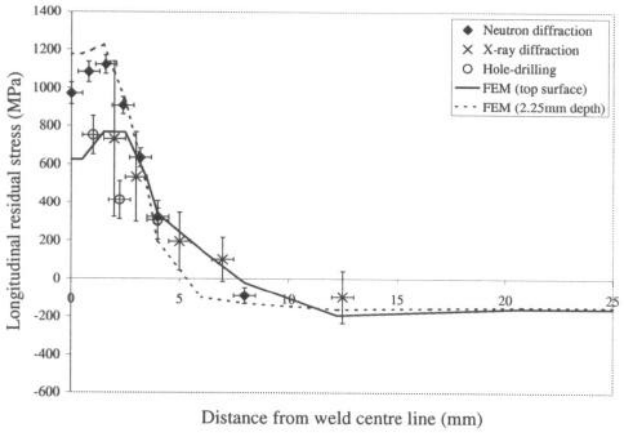

Figure 13: Plot of the measured and predicted longitudinal stress as a function of distance from the weld centre line.

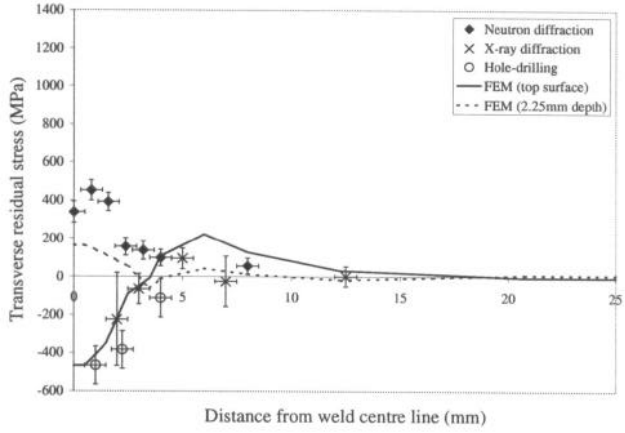

Figure 14: Plot of the measured and predicted transverse stress as a function of distance from the weld centre line.

In Figure 13, large tensile stresses are seen in the longitudinal direction in the vicinity of the weld. These stresses decrease in magnitude with increasing distance from the centre line, becoming compressive in the far field. As discussed earlier, smaller peak stresses are observed at the surface of the sample than at depth. Good agreement is seen between the measurements made with the X-ray diffraction and hole-drilling methods and also with the predictions made by the numerical model at the surface of the sample. Similarly, the measurements made by neutron diffraction are seen to lie between the two lines plotted from the numerical model as expected.

With the transverse residual stresses the numerical model predicts that little or no stress exists in the far-field away from the weld (Figure 14). As the weld is approached, small tensile stresses (~200 MPa) are predicted at the surface of the sample giving way to compressive stresses in and immediately adjacent to the weld. Reasonable agreement is seen between this model prediction and the results obtained by X-ray diffraction and incremental hole-drilling. A different pattern of behaviour is predicted at greater depths into the sample; the stresses are predicted to remain approximately zero up to the weld, after which tensile stresses develop. Again, this behaviour is replicated by the experimental measurements, however, considerably larger stresses are measured in the vicinity of the weld than are predicted by the numerical model. It is likely that this discrepancy arises as a result of the strong crystallographic texture present in the fusion zone. In this region, the lack of crystallites which fulfil Bragg diffraction criteria results in a reduced contribution to the measured reflection from this region. The effect will therefore be similar to the partial immersion of the gauge volume in the sample and will lead to an artificial and systematic shift of the results into tension [17]. If such an effect is indeed being encountered, the magnitude of both the longitudinal and transverse residual stresses may be in error in this region. In both cases it is possible that the actual stress may be smaller than shown.

Comparison between the predictions made for the other beam defocuses showed only small variations between the residual stress profiles at these depths. Indeed, the differences that were observed were smaller than the errors associated with the residual stress measurements given in Figures 13 and 14.

The measured and predicted angular distortions along the length of each of the plates in the investigation of beam defocus are shown in Figures 15 and 16 respectively. In all cases, the angular distortion is seen to remain approximately constant over the majority of the plate with slight variations at the edges arising as a result of the change in constraint on the weld in these regions. The magnitude of the angular distortion can be seen to increase as the defocussing of the electron beam is increased. This behaviour is displayed more clearly in Figure 17 in which the angular distortion obtained from the centre of each plate is plotted against the defocus at which it was welded. It can be seen that the minimum distortion condition is achieved with a slightly overfocussed electron beam. As the defocus is increased from this condition, a corresponding increase in the angular distortion is also observed, with the largest distortions being generated with the greatest defocuses of the electron beam. This behaviour arises as more material is melted above the neutral axis of the test pieces than below it. The subsequent transverse contraction of this material on solidification and cooling pulls the upper half of the weld together by a greater amount than the lower half and hence gives rise to a positive angular distortion, the magnitude of which is dictated by the asymmetry of the weld pool through the thickness of the test piece. Thus those welds which exhibit the greatest asymmetry also display the greatest angular distortion.

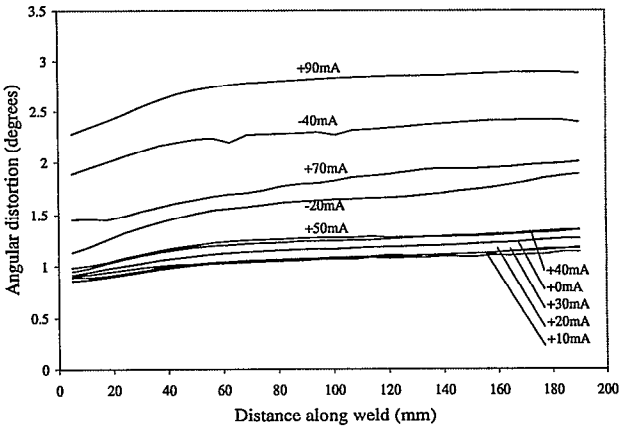

Figure 15: Plot of the angular (butterfly) distortions measured from the samples welded at different defocusses of the electron beam.

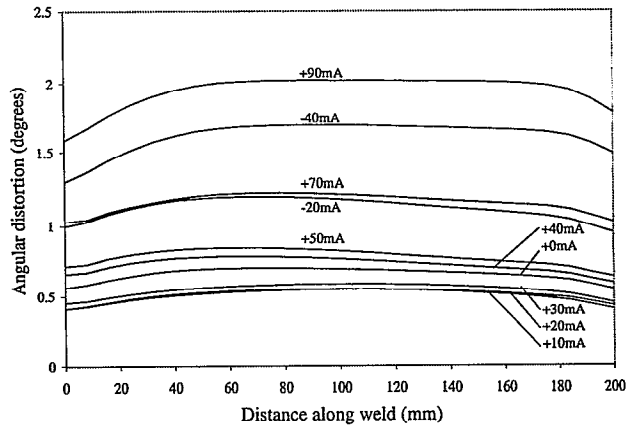

Figure 16: Plot of the angular (butterfly) distortions calculated with the numerical model for each of the samples welded at different defocusses of the electron beam.

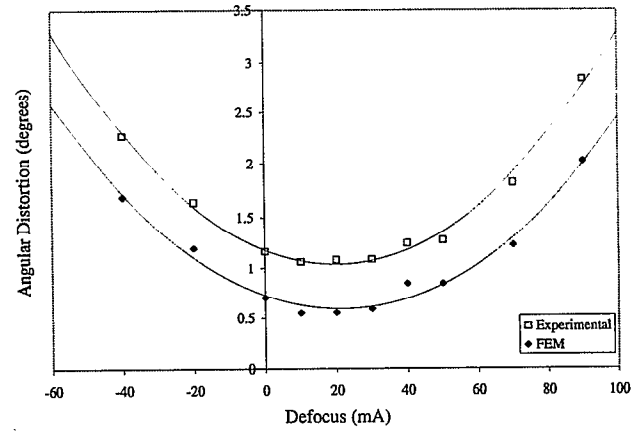

Figure 17: Plot of the measured and predicted angular (butterfly) distortions at the centre of the bead on plate test pieces as a function of the defocus of the electron beam. The lines are a guide to the eye only.

Beyond the range of defocusses investigated, it may be expected that the magnitude of the angular distortions will decrease again as the more diffuse electron beams produced will lead to a reduction in the penetration of the beam and a shallower weld pool.

It can be seen from Figure 17 that whilst the numerical model adequately captures the trends in this distortion mode, it underpredicts the magnitude of this distortion and as will be seen later, overpredicts the magnitude of the camber distortion.

Plots of the measured and predicted camber deflection of the plates along the length of the weld are presented in Figures 18 and 19 respectively. Whilst a systematic variation in this distortion mode is predicted with the numerical model, no such systematic variation is evident in the experimentally determined data. Indeed, it can be seen that adjacent plates in the defocus series exhibit camber distortions that are of the opposite sense, *i.e.* n-shaped rather than u-shaped. The corresponding camber distortions predicted by the numerical model show only u-shaped distortion patterns. These variations may be observed more readily in Figure 20 which shows the peak deflection along each weld as a function of the defocus of the electron beam.

If such distortion arises principally as a result of the differential transverse shrinkage of the weld pool through the thickness of the work piece then it would be anticipated that only a u-shape camber distortion would result, as all of the welds investigated display larger proportions of the weld pool above the neutral axis of the plate than below it. Indeed, at the largest defocuses of the electron beam where the most asymmetric welds are produced, u-shaped camber distortion patterns are observed. It therefore appears likely that the plates welded with more highly focussed electron beams are subject to an instability condition. The numerical model cannot predict such behaviour and poor agreement must necessarily be accepted for these welding conditions.

It was observed from the predicted residual stresses across the top surface of the plates that the variations in the distributions produced at the various defocuses of the electron beam were smaller than the estimated errors associated with the measurements. In contrast, the variations in the distortions produced with the different focal positions of the electron beam were sufficiently large to be measured reliably. It is therefore suggested that the measured post-welding distortion offers a more rigorous test of such a numerical model than the residual stresses.

Summary and Conclusions

The details of a numerical model suitable for the prediction of residual stresses and distortion arising from electron beam welding of aeroengine components has been described. From this work, the following conclusions have been drawn:

1. The magnitude and extent of the residual stresses predicted by the numerical model were shown to be in rea-

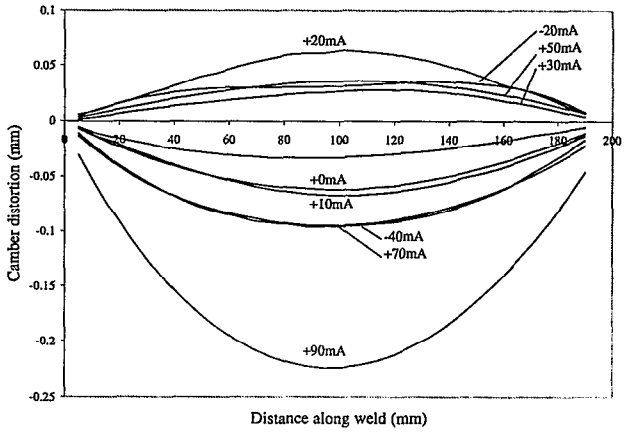

Figure 18: Plot of the camber distortions measured along the samples welded at different defocusses of the electron beam.

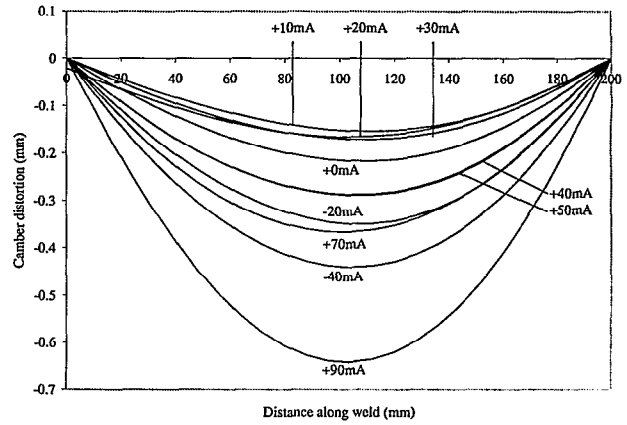

Figure 19: Plot of the camber distortions calculated with the numerical model along each of the samples welded at different defocusses of the electron beam.

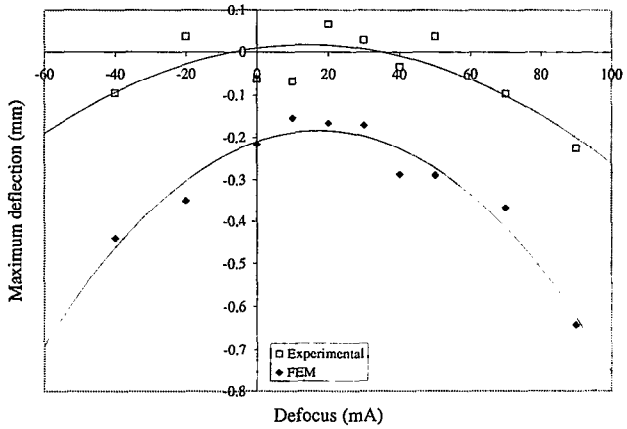

Figure 20: Plot of the peak deflection in the camber distortion mode measured and predicted from the samples welded at different defocusses of the electron beam. The lines are a guide to the eye only.

sonable agreement with those obtained experimentally. As expected, a peak residual stress of the order of the uniaxial yield strength of the material was observed in the longitudinal direction in the vicinity of the weld. The focal position of the electron beam is predicted to have only a small effect on the surface residual stress distribution.

2. The angular distortion generated by this welding process shows a systematic variation with the degree of defocus of the electron beam. A minimum distortion condition was achieved with a slight over-focussing of the beam. The numerical model was found to replicate this behaviour in form, with the predictions being approximately half of their experimentally determined counterparts.

3. The sign of the camber distortion was found to be either positive or negative, with little systematic variation being displayed. This was particularly true for welds made near the normal focus. This was caused by an instability condition arising from the near-uniform deposition of energy through the workpiece. The model as currently formulated is incapable of predicting this phenomenon.

4. The computer simulation of welding processes now provides a virtual capability for the prediction of residual stresses and distortion. However, it is believed that further efforts are required to improve the accuracy of the predictions. This will be possible as computer hardware and software mature.

Acknowledgements

This work was sponsored by the Engineering and Physical Sciences Research Council (EPSRC), Rolls-Royce plc and the Defence & Evaluation Research Agency (DERA). The support of Steve McKenzie & Paul Spilling (Rolls-Royce) and Mike Winstone & George Harrison (DERA) is appreciated. Helpful discussions over a number of years with Moyra McDill, Alan Oddy and John Goldak at Carleton University, Ottawa, Canada are acknowledged.

References

1. H. Schultz, Electron Beam Welding (Abington Publishing, Abington Hall, Cambridge, England, 1993).
2. Edited by J. F. Lancaster, The Physics of Welding (Pergamon Press, Headlington Hill Hall, Oxford, UK, 2nd edition, 1986).
3. H. Schwarz, "Mechanism of high-power-density electron beam penetration in metal", Journal of Applied Physics, 35(7) (1964), 2020–2029.
4. ASM Handbook Volume 6: Welding, Brazing and Soldering (ASM International, 10th edition, 1993).
5. J. H. Argyris, J. Szimmat and K. J. Willam, "Computational aspects of welding stress analysis", Computer Methods in Applied Mechanics and Engineering, 33 (1982), 635–666.
6. J. Goldak, M. McDill, A. Oddy, R. House, X. Chi and M. Bibby, "Computational heat transfer for weld mechanics", In S. A. David, editor, Advances in Welding Science and Technology - Proceedings of an International Conference on Trends in Welding Research, (ASM International, 1986), 15–20.
7. J. Goldak, V. Breiguine and N. Dai, "Computational weld mechanics: A progress report on the ten grand challenges", In H. B. Smart, J. A. Johnson, and S. A. David, editors, Trends in Welding Research - Proceedings of the 4th International Conference, (ASM International, 1995), 5–11.
8. S. M. Roberts, H. J. Stone, J. M. Robinson, P. J. Withers, R. C. Reed, D. R. Crooke, B. J. Glassey and D. J. Horwood, "Characterisation and modelling of the electron beam welding of Waspaloy", In H. Cerjak, editor, Mathematical Modelling of Weld Phenomena 4, (The Institute of Materials, 1998), 631–648.
9. A. S. Oddy, J. M. J. McDill and J. A. Goldak, "Consistent strain fields in 3D finite element analysis of welds", Journal of Pressure Vessel Technology, 112 (1990), 309–311.
10. O. C. Zienkiewicz and R. L. Taylor, The Finite Element Method: Solid and Fluid Mechanics, Dynamics and Non-linearity, volume 2, (McGraw-Hill Book Company, Maidenhead, Berkshire, England, 4th edition, 1994).
11. Edited by E. Hinton, NAFEMS Introduction to non-linear finite element Analysis, (NAFEMS, Birniehill, East Kilbride, Glasgow, UK, 1992)
12. H. J. Stone, P. J. Withers, T. M. Holden, S. M. Roberts and R. C. Reed, "Comparison of three different techniques for measuring the residual stresses in an electron beam-welded plate of Waspaloy", Metallurgical and Materials Transactions A, 30A (1999), 1797–1808.
13. H. J. Stone, T. M. Holden and R. C. Reed, "On the generation of microstrains during the plastic deformation of Waspaloy", Acta Materialia, 47(17) (1999), 4435–4448.
14. M. R. Daymond, M. A. M. Bourke, R. B. Von Dreele, B. Clausen and T. Lorentzen, "Use of Rietveld refinement for elastic macrostrain determination and for evaluation of plastic strain history from diffraction spectra", Journal of Applied Physics, 82(4) (1997), 1554–1562.
15. H. J. Stone, T. M. Holden and R. C. Reed, "Determination of the plane specific elastic constants of Waspaloy using neutron diffraction", Scripta Materialia, 40(3) (1999), 353–358.
16. ASTM E 837, "Standard Test Method for Determining Residual Stresses by the Hole-Drilling Strain-Gage Method", 1994.
17. Edited by J. Lu, Handbook of measurement of residual stresses (The Fairmont Press, 700 Indiana Trail, Lilburn, GA, US, 1996)